Report No: NM98STR-02

New Mexico DEPARTMENT OF TRANSPORTATION
MOBILITY FOR EVERYONE

RESEARCH

New Mexico DOT
Research Bureau
7500 Pan American Fwy
P.O. Box 91750
Albuquerque, NM
87199-4690

HIGHWAY BRIDGE RESEARCH CENTER FINAL REPORT— PHASE I

Prepared by:
Ken White
Rola Idriss
Clint Woodward
David Jaurgui
New Mexico State University

Prepared for:
New Mexico State Highway &
Transportation Department
Research Bureau

In Cooperation with:
The U.S. Department of Transportation
Federal Highway Administration

2005

1. Report No.	2. Government Accession No.	3. Recipient's Catalog No.
NM98STR-02		

4. Title and Subtitle	5. Report Date
Highway Bridge Research Center Final Report – Phase I	January 2005
	6. Performing Organization Code

7. Author(s)	8. Performing Organization Report No.
Ken White, Rola Idriss, Clint Woodward, David Jauregui	

9. Performing Organization Name and Address	10. Work Unit No. (TRAIS)
Bridge Research Center New Mexico State University Box 30001, MSC 3CE Las Cruces, NM 88003-8001	11. Contract or Grant No. CO 4285

12. Sponsoring Agency Name and Address	13. Type of Report and Period Covered
Research Bureau New Mexico Department of Transportation 7500 East Frontage Road P.O. Box 94690 Albuquerque, NM 87199-4690	Final Report 2001 - 2005
	14. Sponsoring Agency Code

15. Supplementary Notes

David Albright, NMDOT Research Bureau Chief; Rais Rizvi, NMDOT Research Engineer;

16. Abstract

The objective of this research was to demonstrate the effectiveness and feasibility of nondestructive testing and monitoring techniques for highway bridges. The work include Fiber Optic Sensor Development where photonics instruments, fiber optic splicing and repair equipment and qualified fiber optics technicians to enable the preparation and installation of fiber optic sensor networks, evaluation of commercial systems including WIM, and the construction of prototype systems as needed.

It also prepared sets of guidelines for installation of fiber optic sensors on existing bridges and new bridges. The work evaluated commercially-available software for combining individual digital images of a bridge site into a single panoramic image and for subsequently viewing it. Evaluate commercially-available PC-based software and digital technology for obtaining high resolution images of structures and processing them into three-dimensional computer models to provide information such as vertical and horizontal clearances or dead and live load deflections. Evaluate the performance of high frequency (>50 kHz) Rayleigh wave ultrasonics generated by piezoelectric transducers to characterize near-surface microcracking.

17. Key Words:	18. Distribution Statement
nondestructive testing, monitoring; damage evaluation; load rating	Available from NMDOT Research Bureau

19. Security Classif. (of this report)	20. Security Classif. (of this page)	21. No. of Pages	22. Price
None	None	40	

HIGHWAY BRIDGE RESEARCH CENTER
FINAL REPORT – PHASE I

Presented to the New Mexico Department of Transportation and the
Federal Highway Administration

Prepared by Ken White, Head of Civil Engineering
Rola Idriss, Professor
Clinton Woodward, Professor
David Jauregui, Associate Professor
New Mexico State University
Las Cruces, New Mexico

Background:

To be recognized as a transportation leader, The New Mexico Department of Transportation (NMDOT) is committed to implementing innovative ideas (Compass 16c). To help achieve this result, in March 2002 a center for research in advanced sensors and bridge inspection technology that integrates data from structural monitoring, nondestructive testing and load testing into reliability index ratings of bridge conditions was established at New Mexico State University (NMSU) through combined funding of the NMDOT and the Federal Highway Administration , FHWA.

New Mexico State University was chosen as the lead on the research team for the area of structures within New Mexico and home for the Highway Bridge Research Center (Center). The Center did undertake the research topics listed below in accord with the priorities established in the Strategic Plan and annual Work Plans.

Research Tasks:

The following research tasks were identified in the Strategic Plan and confirmed by the Research Advisory Committee for the Center.

1. Fiber Optic Sensor Development
   A. Establish a fiber optic sensor laboratory with the necessary photonics instruments, fiberoptic splicing and repair equipment and qualified fiber optics technicians to enable the preparation and installation of fiber optic sensor networks, evaluation of commercial systems including WIM, and the construction of protoype systems as needed.
   B. Prepare sets of guidelines for installation of fiber optic sensors on:
      a. existing bridges
      b. new bridges

C. Develop draft standards for Bragg grating or other types of fiber optic sensors covering such aspects as:
    a. gage length
    b. sensor spacing on fiber
    c. nominal fiber lengths
    d. sensor center wavelengths
    e. coatings
    f. connectorization
D. Develop and implement tests for evaluating durability of fiber optic sensors.
E. Investigate innovative photonic technologie5 for higher sampling rates.
F. Develop telecommunications systems and data protocols including wireless and/or optical systems for real time data acquisition at remote sites.
G. Research advanced mathematical techniques and algorithms for extracting information on bridge condition and traffic monitoring from fiber optic sensor networks.
H. Investigate applications of fiber optics for sensing other variables besides longitudinal strains, such as pressure, temperature, moisture etc.

2. Virtual Reality Methods for Bridge Inspection

A. Evaluate commercially-available software for combining individual digital images of a bridge site into a single panoramic image and for subsequently viewing it.
B. Evaluate commercially. available wearable computer technology that can be used by bridge inspectors in the field for obtaining digital images, displaying virtual reality views and annotating them electronically.
C. Develop standard formats and procedures for incorporating virtual reality files in bridge management data bases.

3. Close Range Photogrammetry

A. Evaluate commercially-available PC-based software and digital technology for obtaining high resolution images of structures and processing them into three-dimensional computer models to provide information such as vertical and horizontal clearances or dead and live load deflections.
B. Develop software for automatically detecting, classifying and quantifying damage such as cracks in three-dimensional photogrammetry image data bases.
C. Evaluate innovative imaging technology such as infra-red cameras that can supplement and enhance visible wavelength imaging photogrammetry

4. Ultrasonic Nondestructive Test Of Concrete Deterioration

A. Prepare reinforced concrete slab test specimens with known amounts of microcracking damage.

B. Evaluate the performance of high frequency (>50 kHz) Rayleigh wave ultrasonics generated by piezoelectric transducers to characterize near-surface microcracking.
C. Evaluate the performance of low frequency (10-50 kHz) Rayleigh wave ultrasonics generated by the impact method to characterize microcracking at depth.
D. Conduct field tests of Rayleigh wave method on damaged concrete bridge decks to determine operational characteristics.
E. Evaluate the performance of advanced transducers such as lasers or micro-electro-mechanical (MEM) sensors for generating or detecting Rayleigh or other modes of ultrasonic waves.

5. Load Factor Calibration and Analysis
   A. For a selected set of bridge structures conduct load testing using strain gage and deflection sensors at selected intervals for shape sensing to determine load factors according to the proposed AASHTO Manual for Condition Evaluation and Load Rating of Highway Bridges.
   B. Analyze the load test data to identify which structural factors are the most significant for determining the shape and its variation.
   C. Evaluate the performance of the AASHTO Virtis software for determining load ratings.

Results of the Research Activity:

The results of the each tasks is described below. Several publications are identified with the various tasks and are identified for the benefit of those interested in more detailed information of that specific research activity.

1. Fiber Optic Sensors:

This project has been delayed by construction delay. The sensor are now installed and initial data recorded but the results and analysis will be conducted as information is available. The overall objective of a monitoring system is to provide a useful, efficient global bridge inspection tool via the network of embedded sensors. The monitoring system design should have an overall systems approach. The lay out for the placement of sensors should be based on an in depth knowledge of the structural behavior of the bridge. The performance of the fiber optic monitoring system in the field needs to be evaluated based on its ability in addressing the issues that have been recognized as priority for maintenance and inspection of bridge structures. Such a system can be used for diagnostic testing, or performance monitoring of the bridge.

Fundamental issues relevant to the installation of a full scale fiber optic bridge monitoring system are being considered, such as:

- Sensor type,

- Embedment requirements,
- Needed instrumentation,
- Number of sensing locations
- Ease of use and embedment operations during construction,
- Simplicity of operations during monitoring.

Data collected from several bridge projects is being considered and guidelines for installation of fiber optic strain sensors will be prepared based on previous research conducted on bridges in New Mexico.

2. Virtual Reality Methods for Bridge Inspection:

This section describes the use of Quick Time Virtual Reality (QTVR) for the documentation of routine inspections. The amount of equipment needed for a virtual reality system is not extensive; a basic system (excluding a laptop computer) should include a high-resolution digital camera, a camera tripod, panoramic tripod heads, and virtual reality computer software. The virtual reality documentation process consists of three basic steps: (1) planning and taking of photographs; (2) creation of panoramas; and (3) rendering of virtual reality records with hot spots. These steps are discussed in the following sections for different bridge inspection projects.

Planning and taking of photographs. The planning of the photographs primarily involves selecting the nodal positions for the camera, which are simply the camera locations at which a panoramic view of the structure is desired. At each nodal position, a series of individual photographs in equal angle increments are taken which will later be merged into a single panoramic image as illustrated in Figure 1(a).

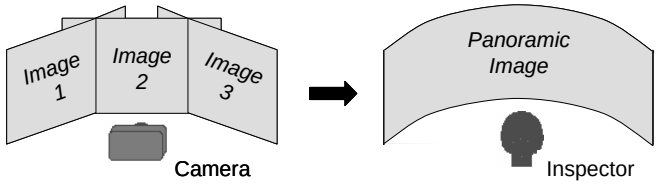

(a)

(b)

Figure 1. Creation of cylindrical panorama: (a) general process and (b) prestressed concrete bridge example.

Acquiring all the images necessary for a complete QTVR record of a bridge may require several field visits. During the first visit, however, the work should focus on acquiring global panoramas of the bridge both in elevation and cross-section. Subsequently, plans should then be made to photograph local areas of the bridge where damage and/or deterioration tend to concentrate. These problem areas should be identified with the assistance of an experienced bridge inspector or professional engineer. Photographs of these local areas will establish a baseline by which future condition assessment will be made.

In general, the inspector should follow good photographic procedures when acquiring the images to be used in the QTVR record. A good quality tripod should be used in order to adjust to the rough terrain encountered at a bridge site. The camera should be oriented vertically so that all photos have a portrait orientation to fill the image area as much as possible. The camera should be positioned on the mount such that the camera rotates horizontally about the focal point of the lens. Panoramic tripod heads have an indexed, graduated rotation scale so that the camera can be rotated in equal angle increments. This ensures that the degree of overlap between the photographs is reasonably constant throughout the series of pictures.

The camera should be set to a timed shutter release mode to avoid camera movement as the pictures are taken. Experience in the field has also shown that auto focus lenses should be set to manual mode. Furthermore, each individual picture should be taken with no moving objects and avoiding changes in lighting conditions, if possible. Blurry pictures, changes in exposure, and moving objects can all cause problems when merging photographs since the stitching software cannot match pixels between images.

Creation of panoramas. There are two main groups of panoramas: cylindrical and cubic. Cylindrical panoramas give the experience of standing in the center of a cylinder and panning horizontally up to 360 degrees. Cubic panoramas add the effect of being able to pan as much as 180 degrees overhead and underfoot in a 3-D

spherical environment. Cylindrical panoramic creation may be done using the VR Worx program (VR Toolbox, 2003). This program performs stitching automatically by identifying and matching pixels between adjacent images. An overlap of 30% is needed in order for the stitching to work properly. Figure 1(b) shows the merging of 8 individual images taken of the underside of a prestressed concrete girder bridge into a single panorama.

Panoramic development may also be done using the RealViz Stitcher program (Realviz, 2004), which has an extremely robust stitching process. An advantage of this program is that pictures can be manually maneuvered until adjacent images are closely aligned; the software further refines the image positions automatically. Another advantage of Realviz Stitcher is that it has the capability for the creation of cubic panoramas. A full 360° cubic panorama requires three separate rows of images taken at vertical angles of -45, 0, and +45 degrees. Figure 2(a) shows the typical camera positioning for the acquisition of images for a cubic panorama. Cubic panorama stitching in Realviz Stitcher is more labor intensive since the images have to be placed into the stitching workspace manually and roughly positioned before the software performs the fine adjustment. Figure 2(b) shows the creation of a cubic panorama of a steel truss bridge in progress.

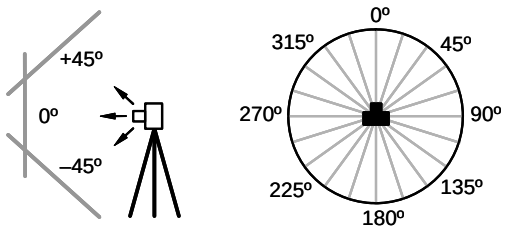

(a)

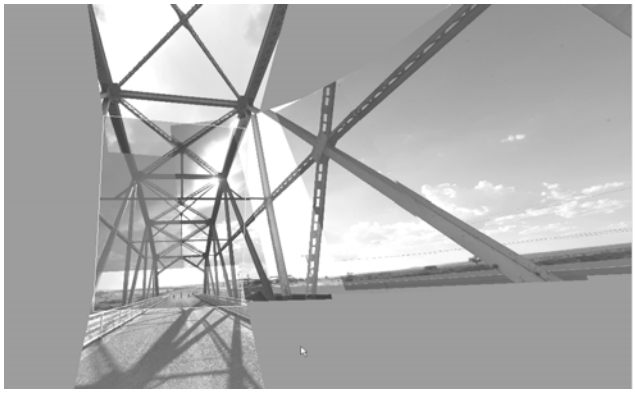

(b)

Figure 2. Creation of cubic panorama: (a) camera setup and (b) steel truss bridge example.

Rendering of virtual reality records with hot spots. Once the stitching process is complete, the cylindrical and/or cubic panoramas are rendered to an output file for viewing on the Apple QuickTime player. In the final virtual reality record, hot spots are used to bring together the rendered panoramas and discrete photographs of local areas (prone to or with existing damage and/or deterioration). Generally speaking, hot spots are user-defined links that connect (1) separate panoramas and/or (2) a panorama to a single picture; a nodal map defines the interaction between a single panorama and its associated links. Written explanations along with design drawings and maps may be included to fully describe the view within the virtual bridge environment and/or the specific bridge feature under observation. The amount of office time spent in the development of a virtual bridge record will depend on several factors such as (1) the number and type of panoramas; (2) the number of hot spots or links; and (3) the amount of miscellaneous material such as local pictures, text descriptors, design drawings and/or maps included in the record.

Figure 3 shows a sample QTVR movie of a steel I-girder bridge. The movie screen has three distinct areas; the header, image, and footer area. The header area of the screen displays the name of the bridge inspection project and also contains the menu bar for the Apple QuickTime player. Below the header, the image area of the screen displays the cylindrical and/or cubic panoramas. Using the computer mouse, the inspector may navigate the panoramic area. User-defined hot spots appear as transparent, outlined regions within the image area which link the active panorama to other panoramas and/or individual pictures. When the cursor is positioned in the delineated area of a hot spot, a narrative appears towards the bottom of the screen in the footer area to describe the link. A simple click of the computer mouse (with the cursor positioned within the hot spot area) will show the linked panorama in the image area; this new panorama is now active and may have associated links of its own. As mentioned earlier, hot spots may also link a panorama to individual pictures of noted problem areas. For instance, clicking on the hot spot on the left side of the image area shown in Figure 3 brings up the picture of a spalled area (with exposed rebar) beneath the curb of the reinforced concrete deck shown in Figure 4. Menu buttons in the footer area of the screen allow the inspector to zoom in and out of the scene, to toggle the display of the hot spots on and off, and to return to the previous panorama and/or individual picture.

Potential Impact and Future Developments. Virtual reality can favorably contribute to bridge inspection practice in several possible ways. First of all, inspectors will often review information given in past reports to determine the type and severity of previously observed damage and/or deterioration to prepare for an upcoming bridge inspection. Design drawings, field sketches, and/or still photographs are also reviewed to further aid the inspector. Following the inspection, the observed bridge condition is then evaluated relative to that previously recorded to determine if there are any changes. This comparison may be troublesome due to the written format and limited amount of photographic documentation given in a typical inspection report. In

a virtual reality system, notes and photographs can be integrated into an interactive and more realistic visual environment to aid in tracking changes from inspection to inspection.

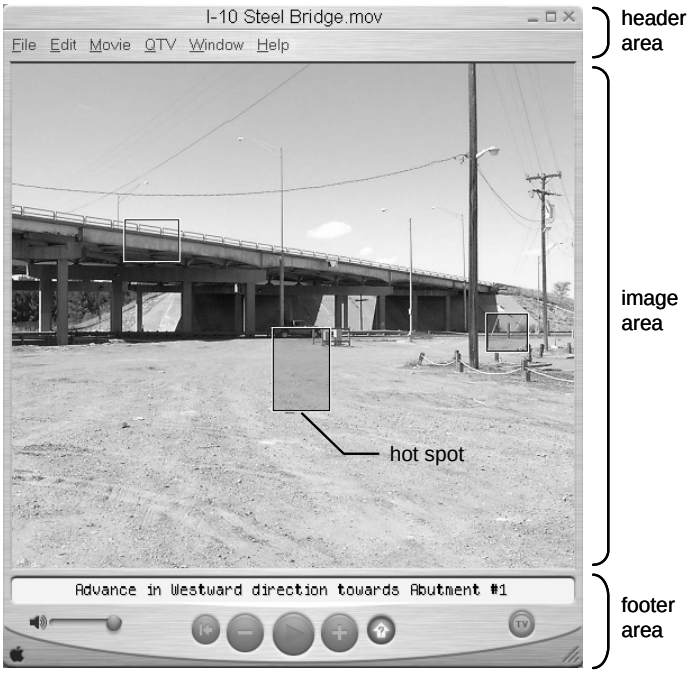

Figure 3. Virtual reality record of steel girder bridge showing screen areas.

Figure 4. Virtual reality record of reinforced concrete deck showing display buttons.

Another powerful feature of this technology is that design drawings, overhead maps, and/or audio recordings can be integrated into the virtual reality record. In such an application, clickable node markers may be overlaid on the bridge drawing or map at different reference points. Clicking on a node marker then transports the inspector to a linked panorama. As the inspector navigates the panorama, a directional indicator on the active node marker follows the inspector's line of sight to show the position and viewing orientation of the panorama along with an audio description. This particular capability may prove quite useful to acquaint the inspector with the bridge structure and site prior to an inspection. As indicated earlier, consistent and uniform field inspections depend greatly on the experience and training of the inspection teams. The detailed, high-resolution photographic records will allow supervisors to quickly review each inspection without personally visiting every structure. Supervisors will also be able to review inspections with the field crews to improve the quality of the final reports to better determine when critical damage or deterioration has occurred.

Bridge inspector training courses that cover visual inspection could benefit greatly from virtual reality technology. In order to fulfill NBIS training requirements, inspectors must complete a comprehensive training course. These courses are offered

by various agencies and cover general topics such as bridge mechanics; bridge materials; bridge types and components; fundamentals of bridge inspection; and bridge inspection reporting. Also covered in depth are the inspection and evaluation of bridge decks; timber, concrete, and steel superstructures; fracture critical bridge members; bridge bearings; and substructures. As part of the course, participants are asked to review as-built drawings, previous inspection reports, and photographs for various case studies. Alternatively, this bridge condition data could be put together for examination in a virtual reality setting, thus, making the inspection exercise much more valuable and realistic. Certainly, time must be allotted in any practical oriented training course to include hands-on field inspections at the actual bridge site; however, in an interest of time, only so many can be made. Virtual bridge inspections cannot replace but can definitely help the inspector gain valuable additional field experience without having to leave the classroom. Also, on-the-job training by supervisors and more experienced inspectors could be accomplished by this method.

A major concern in adopting a virtual reality approach for documenting bridge inspection projects is that the size of the final output files can be quite large. A possible way to address this issue is to post the virtual reality files on the Internet. When the Apple QuickTime Player is installed, plug-in drivers are automatically loaded for the Netscape and Internet Explorer browsers so that virtual reality content may be viewed over the web. This means that several smaller sized panoramas may be linked together with a web browser rather than having all the panoramas on a single, large file. Web-based applications also make it possible to manage conventional bridge inspection forms. Internet files can also be accessed by supervisors or bridge experts when needed without visiting the site. In fact, the integration of virtual bridge inspections and the Internet provides a vast array of possibilities for further development.

An important final note about virtual reality is that the field work may be challenging for some bridges. For example, bridges located in areas of heavy traffic or crossing a river may need to be closed or require traffic control to perform the photography. Furthermore, a river crossing may require special equipment to position the inspector underneath the bridge to take pictures. Bridge sites having other forms of moving obstructions (such as those located in construction zones) are also demanding candidates for virtual reality since the photography must be carried out during periods of either low or no construction. To summarize, situations where traffic control, bridge closure, and/or special equipment rental is needed will demand more of a time investment and also result in higher inspection costs compared to that of a typical inspection.

References

American Association of State Highway and Transportation Officials (AASHTO) (2000), *Manual for condition evaluation of bridges*, 2nd Edition, Washington, AASHTO.

Federal Highway Administration (FHWA) (1995), *Recording and coding guide for the structure inventory and appraisal of the nation's bridges*, Washington, United States Department of Transportation.

Realviz (2004), *The Stitcher user manual*, Version 4.0, Valbonne, Realviz.

Rolander D D, Phares B M, Graybeal B A, Moore M E, and Washer G A (2000), 'Highway bridge inspection: state-of-the-practice survey', *Transportation Research Record*, 1749, 73–81.

Phares B M, Graybeal B A, Rolander D D, Moore M E, and Washer G A (2000), 'Reliability and accuracy of routine inspection of highway bridges', *Transportation Research Record*, 1749, 82–92.

VR Toolbox (2003), *The VR Worx user manual*, Version 2.5, Pittsburgh, VR Toolbox.

3. Close Range Photogrammetry:

Photogrammetric surveying is a method where three-dimensional measurements are made from two-dimensional photographs taken of an object. In general, photographs are taken of an object from at least two camera positions. From each camera position, there is a line of sight that travels from each visible point on the object to the perspective center of the camera. Using the principle of triangulation, the point of intersection between the different lines of sight for a particular point is determined mathematically to identify the spatial location of the object point. Photogrammetry may be classified as either aerial or terrestrial. In aerial photogrammetry, photographs are taken overhead from an aircraft while in terrestrial photogrammetry, the photographs are taken from stations situated near the earth's surface. When pictures are taken of an object within the range of 100 mm (4 in) to 100 m (330 ft), photogrammetry is further defined as close-range terrestrial photogrammetry (Hilton, 1985).

There are four basic steps in the photogrammetric process: layout of the control network, planning and taking the photographs, processing the photographs, and point measurement using the photographs (Hilton, 1985). Control points with known spatial coordinates are used to establish a reference system between the photographs and the real structure. Cameras built specifically for photogrammetric surveying purposes (in particular, aerial surveys) are defined as metric cameras. The interior configuration of this type of camera is very stable and as a result, metric cameras are generally more expensive than semi-metric cameras. The camera used in this research is a KODAK DCS 660 semi-metric, digital camera with a 6-megapixel (3000 x 2000) resolution and equipped with a 28-mm wide-angle lens. For photogrammetric use, this camera must first be calibrated to determine internal parameters such as lens distortion and focal length. Processing and measurement of the photographs is done using FotoG, a photogrammetry software program developed by Vexcel (2000).

Close-range photogrammetry has found a number of applications in both the engineering and nonengineering communities. Industrial inspection, architectural documentation, and forensic analysis are three modern applications of close-range photogrammetry. In the field of structural engineering, close-range photogrammetry has been used to measure, model, monitor, and/or document the thermal deformation of steel beams (Fraser and Riedel, 2000); the local flange buckling of curved, steel box girders (Scott, 1978); the shape of soil-steel structures (Bakht and Maheu, 1994); the laboratory deformation of a closed-spandrel arch bridge up to failure (Forno et al., 1991); the appearance of historic transportation sites (Spero, 1983); the deformation of concrete beams and columns under laboratory loading (Fraser and Brizzi, 2002; Woodhouse and Robson, 1994; Whiteman et al., 2002); the characteristics of highway roadside features (Nastasia, 1998); and the shape of space structures in stationary, vibrating, and deploying conditions (Pappa et al., 2002). Short-term and long-term

photogrammetric measurement of in-service bridges have been carried out in various bridge engineering applications by Bales (1984), Kim (1989), Johnson (2001), Albert et al. (2002), Cooper and Robson (1990), and Jáuregui et al. (2003).

Field Study 1: Prestressed Concrete Girder Bridge. Field evaluation of the photogrammetric measurement system was first carried out during a new bridge construction project in Las Cruces, New Mexico (Jáuregui et al., 2003). The single-span, prestressed concrete bridge (designated as the Las Alturas Bridge) is 32.2 m (105 ft) long with an 18º skew. The superstructure consists of five BT-1600 (BT-63) bulb-tee girders spaced at 2.90 m (9.5 feet) and supporting a 230-mm (9-in) reinforced concrete deck. The bridge girders are numbered from 1 to 5 from west to east and span 31.1 m (102 feet). There is a 0.81-m (32-in) barrier rail on each side of the deck. Photogrammetric measurements were made to determine (1) the initial girder camber and (2) the girder deflection caused by the weight of the concrete deck and traffic barriers.

Photogrammetric targets were mounted on the east side of the bottom flange of each girder. The bullseye targets were installed at five points along the length of each girder: the ends, the quarter points, and mid-span for a total of 25 targets. These girder targets are hereafter referred to as tie points. A total of 15 control points were mounted on the abutments and retaining walls at both ends of the bridge. Figure 5 shows the locations of control points on the south end of the bridge along with some of the tie points on the girders.

Figure 5. Locations of tie and control points on Las Alturas Bridge.

Care was taken to distribute the control points throughout the entire area of the bridge at positions assumed to be rigid relative to the superstructure. Hence, any small displacements that may have occurred at these points were neglected. Control information was obtained by surveying the control points with a total station and prism. The measurement accuracy of the total station is approximately 1.5 mm (0.005 ft) with a 1-second resolution for angles. A

Cartesian coordinate system was established with the northeast corner of the bridge as the origin. Recorded data from the total station included the distance and angle to the control points from an established baseline. These measurements were then transformed into the Cartesian coordinate system to give the x, y, and z coordinates for each control point.

Two sets of photographs were taken at an average distance of approximately 18 m (60 ft); one before the casting of the deck and barriers with the girders in their undeformed cambered positions and the other after with the girders in their deformed positions under dead load. Photographs were taken looking in three different directions. First, a strip of photographs was taken moving north to south with the camera on the east side of the bridge looking west. The second and third strips of photographs were taken moving east to west underneath the bridge along the centerline and looking northwest and southwest, respectively. With the targets placed on the east side of the girders, pictures could only be taken in the westward direction. Dead load deflections were computed by subtracting the coordinates determined from the picture sets before and after loading.

Photogrammetric measurements of the initial camber were compared to those obtained using a traditional surveying level. Level readings were taken at tenth points with a rod positioned on the girder top flanges. Variation of these measurements occurred due to the surface irregularities of the girder top flanges. Figure 6 shows a typical comparison between the photogrammetric measurements, labeled **DCRTP**, and level rod readings, labeled **Level (Data)**. On the horizontal axis, the longitudinal location ranges from 0.0 m (the north end) to 31.1 m (the south end) along the girder length. A curve fit analysis was performed on the level rod readings resulting in the solid line labeled **Level (Fit)**. Compared to the fitted curves, the photogrammetric measurements were within a standard deviation of ± 8.5 mm (0.33 in) for girder 1, ± 2.4 mm (0.10 in) for girder 2, and ± 13.3 mm (0.52 in) for girder 3, amounting to approximately 1 to 10 percent of the maximum measured girder camber.

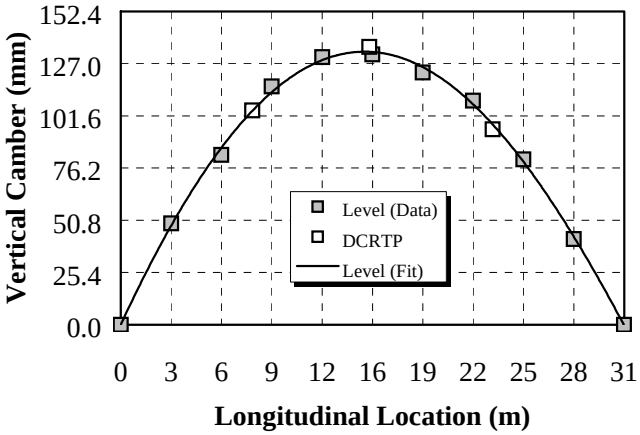

Figure 6. Typical comparison between photogrammetric measurements and level rod readings.

Dead load deflection measurements of the five girders using photogrammetry were evaluated by means of comparison with the dead load deflection (DLD) diagram specified in the design plans. The DLD diagram represents the expected dead load deflection of the bridge beams under the weight of the concrete deck and barriers and is used to set the rails for the screed to ensure that the deck is level after casting. The dead load deflections for the five girders are plotted in Figure 7 along with the DLD diagram. The standard deviation was approximately ±2.9 mm (0.11 in) at the first quarter point, ±3.2 mm (0.13 in) at mid-span, and ±5.4 mm (0.21 in) at the third quarter point. Differences of this magnitude were expected since the DLD diagram is based on assumed material properties and a constant deck thickness. In addition, the boundary conditions are assumed to be simple supports and the contribution of the prestressing steel to the moment of inertia is ignored.

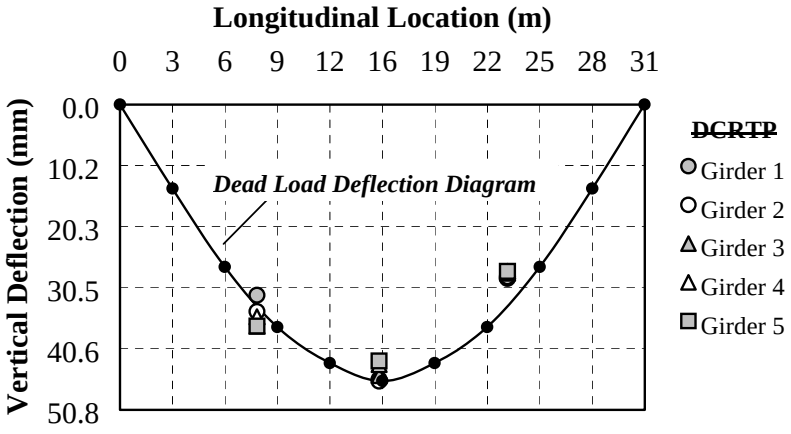

Figure 7. Comparison of photogrammetric measurements and dead load deflection diagram.

Field Study 2: Non-Composite Steel Girder Bridge. The second field evaluation of the photogrammetric measurement system was conducted on a steel girder bridge designated as the Alamosa Canyon Bridge (Jáuregui et al., 2003). The objective of this study was to evaluate the measurement of live load girder deflections by photogrammetry. The Alamosa Canyon Bridge was built in 1937 and consists of seven simple-supported, non-composite, slab-on-girder spans. The bridge crosses the Alamosa Canyon, a normally dry arroyo that carries runoff to the nearby Rio Grande River, about 16 km (10 miles) north of the town of Truth or Consequences, New Mexico. In 1967, the bridge was retired from service and replaced with twin prestressed concrete bridges to carry north and southbound traffic on Interstate 25. Since 1994, the NMSU Civil Engineering Department has used the original Alamosa Canyon Bridge for bridge-related research because of its excellent accessibility and historic construction type.

A load test was performed on one of the interior spans of the Alamosa Canyon Bridge. This span, similar to the other six, is 14.9 m (49 ft) long with six CB30x116 (similar to a W30x116 wide flange by current AISC standards) steel girders spaced at 1.47 m (4 ft 10 in) on center. The girders are numbered one through six, with one being the westernmost girder. The top flanges of the girders are embedded through their thickness into the underside of the 197-mm (7.75-in) thick reinforced concrete deck; however, no shear connectors are provided. For design purposes, the north end of the span was treated as fixed (i.e., no longitudinal movement) and the south end was treated as an expansion support (i.e., longitudinal movement allowed). Reinforced concrete parapets are cast integral with the deck on both sides, and concrete barrier rails are attached to the outside of the parapets.

Based on previous laboratory test results (Jáuregui et al., 2003), it was shown that the use of double-sided targets improved the accuracy of the photogrammetric solution. As a result, steel frames were fabricated to hold double-sided laminated paper targets. Targets were mounted on the bottom flange at the $1/10^{th}$ points of each of the six girders. These 54 targets served as tie points for the photogrammetric solution. Control targets were attached to three points near the top and bottom of the pier wall on the north and south ends of the span. Figure 8 shows the target layout towards the north end of the tested span of the Alamosa Canyon Bridge. All targets were labeled similar in format to that used in the Las Alturas Bridge study. In addition, the same equipment and procedures given previously in the Las Alturas Bridge study were used to survey the twelve control points and determine the control coordinates for use in the photogrammetry analysis.

Figure 8. Target layout towards north end of Alamosa Canyon Bridge.

The tested bridge span was photographed first in its unloaded state and then under loading by two dump trucks (each weighing approximately 250 kN or 56 kips) placed side-by-side. The trucks were centered transversely on the bridge deck with the second axle at mid-length of the span to maximize vertical deflections at mid-span. Photographs were taken from either side of the bridge during both the unloaded and loaded condition with the trucks stationary on the deck. The photography sequence, data processing, and final computation of deflections caused by the trucks followed essentially the same procedures as those used in the Las Alturas Bridge study. A surveying level rod was also used to measure the mid-span deflections of each girder under the applied truck loading.

To have an idea of the expected vertical deflection of the girders, a linear elastic finite element analysis (FEA) was performed to predict the response of the bridge under live load. Although no definite connection was provided between the girder and the concrete deck, behavior between a fully composite and a non-composite section was expected because of the effects of friction and mechanical interlock at the girder-slab interface (Jáuregui et al., 2002). As a result, two finite element models were created to determine the range of expected deflections of the bridge; one having full composite action and one having non-composite action. In addition to the finite element analysis, a diagnostic load test was performed to further evaluate the behavior of the bridge. Strain transducers were attached to the middle of the web and the topside of the bottom flange of each of the steel girders at four longitudinal locations. The strain profile over the depth of each cross-section allowed curvature to be determined along the length of each girder. Based on the loading pattern and assuming linear variation of curvature along the span length, the curvature diagram for each girder was approximated. The conjugate beam method was then used to estimate the girder deflections.

Typical results of the various analysis methods are shown in Figure 9. Elastic FEA results determined based on non-composite action (labeled as **FEM (N-C)**) are depicted with solid gray circles while results based on composite action (labeled as **FEM (Comp)**) are depicted by solid white circles. Photogrammetric results (labeled as **DCRTP (Data)**) are plotted as solid black triangles. A third-order polynomial regression was performed on the photogrammetry data, which resulted in the dashed line labeled **DCRTP (Fit)**. Curvature-based deflections (labeled as **Conjugate Beam**) are plotted using open square symbols while level rod measurements for each girder are labeled **Level Rod** and plotted as an asterisk.

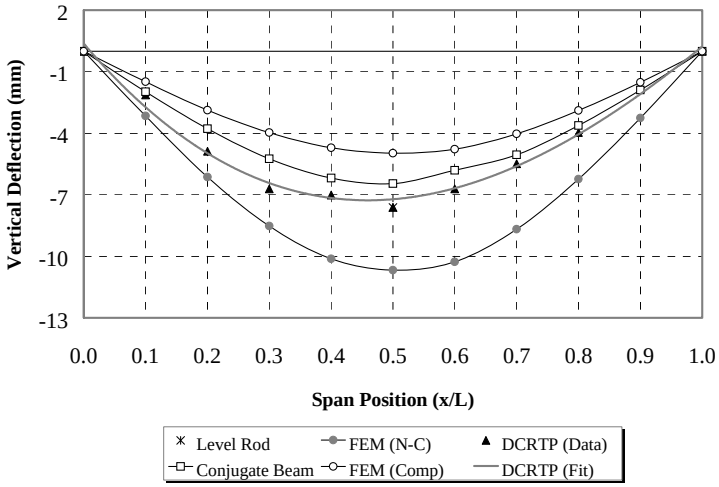

Figure 9. Vertical deflection under live loading versus span position for typical girder.

Note that the composite and non-composite FEA results bracket the experimental results from the photogrammetric, conjugate beam, and level rod deflection values. At midspan, the photogrammetric and conjugate beam calculated deflections were within 1 mm (0.04 in) of one another, while photogrammetric and level rod readings were within 0.5 mm (0.02 in) of one another for all girders. Comparison of the midspan deflections of each girder from the photogrammetric analysis with the two FEA models gave an estimate of the level of composite action. The outer girders 1 and 6 were 92% and 87% composite by this criterion, falling to 71% for girder 2 and 68% for girder 5, and 54% and 58% for the central girders 3 and 4, respectively. The effects of friction and mechanical interlock between concrete and steel along with embedment of the top flange of the girders into the bottom of the deck are most likely the cause of the partial composite action (Jáuregui et al., 2002).

Potential Impact and Future Developments. Much like virtual reality, close-range photogrammetry has tremendous potential in the fields of bridge inspection and monitoring. First of all, a major challenge in the field testing of bridges is the measurement of vertical deflection. The use of instruments such as mechanical dial gages, linear potentiometers, LVDTs (i.e., linear variable differential transformers),

and other similar types of deflection transducers is often difficult since a fixed base is needed from which relative displacements are measured. This may require access under the bridge to erect a temporary support to mount the instrument or for running a wire from the instrument to the ground. Other non-traditional methods have also been employed by agencies such as the Swiss Federal Laboratories for Material Testing and Research, which have successfully used a wire-supported method, a water-leveling method, a horizontal wire-leveling method, and an electronic leveling system for vertical deflection measurement (Ladner, 1985). Compared to these measurement techniques, however, the photogrammetric method has several advantages, a few of which are (1) it is less labor-intensive; (2) it is capable of measuring difficult-to-access structures; (3) a large amount of geometric data can be extracted from the photographs; (4) additional measurements can be taken at a later time without repeating the field work; and (5) it can be used on a routine basis for various measurement applications (Bakht and Maheu, 1994).

Furthermore, photogrammetry is a non-contact technique meaning that measurements are made without having to touch the structure. Other systems are available which provide non-contact measurement capabilities using laser technology, however, at a higher cost. A photogrammetric system can operate at a fraction of the cost of a laser-based system and is thus, perhaps more likely to fit within the budget constraints of a highway agency.

As mentioned earlier, routine bridge inspections are chiefly performed in accordance with highly-subjective visual procedures and are often carried out within high traffic corridors. One of the most time-consuming and frequently dangerous activities in a routine inspection is the measurement of vertical and horizontal clearances. Presently, inspectors must use measuring tapes or rods and often have to do complete this task surrounded by high traffic volumes. As photogrammetry techniques continue to develop, clearance measurements may be made from digital photographs taken from more remote locations away from traffic. A related inspection difficulty is the measurement of cracks, delaminations, and spalls as well as other types of deterioration in locations where access is extremely difficult. Again, photogrammetry techniques can provide the means for a safe and accurate measurement of a deteriorated area.

Another aspect of bridge inspection that may benefit from close-range photogrammetry is the documentation of historic structures, particularly those that may need to be removed or destroyed. Federal regulations require the proper documentation of historic bridges including such aspects as overall geometry, structural deterioration, and historic features. Many photogrammetry software programs have the capability to create three-dimensional, photo-textured models as well as two-dimensional, orthographic photographs (i.e., ortho-photos). Photo-textured modeling allows natural textures to be extracted from the photographs and applied to the surfaces of the three-dimensional model providing a truly realistic

impression of the structure. These models can be exported into virtual reality format for display in still-life or animated format and may also be ultimately posted on the Internet for remote viewing by other interested parties. Ortho-photos represent the projection of a three-dimensional model onto a two-dimensional plane and thus, provide the means for creating as-built drawings of a structure in plan, cross-section, and/or elevation view. Since perspective is removed, ortho-photos have the advantage that they may be directly used for object measurement using the appropriate scale. Both these features allow the structure to be displayed in a much more realistic format and viewed from different directions which can serve to provide a much better understanding and appreciation of the bridge's construction and historical significance.

As with any new technology used for bridge inspection and monitoring, there are certain obstacles that must be overcome for field use and close-range photogrammetry is no exception. Environmental factors such as temperature and humidity variations in the air may contribute to errors in photogrammetric measurement and ways to minimize and/or compensate for these variations must be investigated. One such remedy is to perform the photography close to sunset to help stabilize environmental conditions which can also serve to minimize traffic disruption. Flash photography can be performed using retro-reflective targets and equipping the digital camera with a high-intensity ring light. Another potential way to account for environmental factors is by self-calibrating the digital camera at the bridge site. In a self-calibration, optical parameters such as focal length and lens distortion of the digital camera are determined from points measured on the actual structure and based on the in-situ environmental conditions as well as the true object scale (Atkinson, 2001). Another aspect of photogrammetry in need of further investigation is establishing the control network. The traditional approach of using a total station to obtain three-dimensional coordinate data of control points is extremely time-consuming and prone to measurement errors of its own. Some photogrammetry systems offer the option to perform the bundle adjustment using a free-network solution (with inner constraints established by calibrated scale bars). The former approach could serve to reduce the time spent in the field since bars with known dimensions could be used to establish the control network instead of surveyed points; however, further investigation is needed to determine the level of accuracy of the free-network bundle adjustment. The capability of automated target recognition instead of manual point marking is also provided by some systems which could reduce image processing time, making the use of close-range photogrammetry in bridge applications much more efficient. Finally, professional-grade digital cameras continue to increase in pixel resolution while decreasing significantly in cost. For example, the new Kodak DCS SLR Pro/n digital camera currently (August 2004) provides the industry's highest pixel resolution at 14 mega pixels and is priced approximately one-fifth of that of the Kodak DCS 660 (6 mega pixel resolution) when purchased in the year 2001. With higher resolution cameras, the potential exists for continual improvement in photogrammetric measurement accuracy.

References

Albert J, Maas H-G, Schade A, and Schwarz W (2002), 'Pilot studies on photogrammetric bridge deformation measurement', *2nd International Symposium on Geodesy for Geotechnical and Structural Engineering*, Berlin.

Atkinson K B (2001), *Close range photogrammetry and machine vision*, Scotland, Whittles Publishing.

Bakht B and Maheu J (1994), 'Chapter 10. Distress, monitoring, and repairs,' in Abdel-Sayed G, Bakht B, and Jaeger L G, *Soil-steel bridges: design and construction*, New York, McGraw-Hill Inc, 317–335.

Bales F B (1984), 'Close-range photogrammetry for bridge measurement', *Transportation Research Record*, 950, 39–44.

Cooper M A R and Robson S (1990), 'High precision photogrammetric monitoring of the deformation of a steel bridge', *Photogrammetric Record*, 13 (76), 505–510.

Forno C, Brown S, Hunt R A, Kearney A M, and Oldfield S (1991), 'Measurement of deformation of a bridge by moiré photography and photogrammetry', *Strain*, 27 (3), 83–87.

Fraser C and Brizzi D (2002), 'Deformation monitoring of reinforced concrete bridge beams', *2nd International Symposium on Geodesy for Geotechnical and Structural Engineering*, Berlin.

Fraser C S and Riedel B (2000), 'Monitoring the thermal deformation of steel beams via vision metrology', *ISPRS Journal of Photogrammetry & Remote Sensing*, 55 (4), 268–276.

Hilton M H (1985), *Application of close-range terrestrial photogrammetry to bridge structures*, Report VHTRC 85-R40, Charlottesville, Virginia Highway and Transportation Research Council.

Jáuregui D V, White K R, Woodward C B, and Leitch K R (2003), 'Noncontact photogrammetric measurement of vertical bridge deflection', *ASCE Journal of Bridge Engineering*, 8 (4), 212–222.

Jáuregui D V, Yura J A, Frank K H, and Wood S L (2002), 'Field evaluation of decommissioned noncomposite steel girder bridge', *ASCE Journal of Bridge Engineering*, 7 (1), 39–49.

Johnson G W (2001), 'Digital close-range photogrammetry – a portable measurement tool for public works', *2001 Coordinate Measurement Systems Committee (CMSC) Conference*, Albuquerque.

Kim B-G (1989), *Development of a photogrammetric system for monitoring structural deformations of the sturgeon bay bridge*, PhD Dissertation, Madison, University of Wisconsin.

Ladner M (1985), 'Unusual methods for deflection measurements', *1985 Symposium on Strength Evaluation of Existing Concrete Bridges*, Washington.

4. Ultrasonic Nondestructive Test of Concrete Deterioration.

The average results of the NLUT method over the four paths may be analyzed in several ways. The first methods compare the averaged amplitudes of the fundamental frequency (A_1), the second harmonic (A_2), and the third harmonic (A_3) versus damage. The other methods use variations of the amplitudes A_1, A_2, and A_3. One of these other methods uses the second harmonic amplitude divided by the fundamental amplitude squared versus damage (A_2/A_1^2 versus damage) and the third harmonic amplitude divided by the fundamental amplitude cubed versus damage (A_3/A_1^3 versus damage). Another method plots the second harmonic amplitude versus the fundamental amplitude squared (A_2 versus A_1^2) and the third harmonic amplitude versus the fundamental amplitude cubed (A_3 versus A_1^3). A 95% confidence interval is provided on the plots. The 95% confidence interval is a range of values that has a 0.95 probability of containing future values from the same population.

Additional methods of analysis will include linearization techniques using natural logarithms. An exponential regression function is fitted to the data. For these methods, a correlation coefficient (R^2) value is provided as a means of gauging the effectiveness of the exponential regression fitted to the data. The regression becomes a more reasonable representation of the data as the correlation coefficient approaches unity.

Normalized Harmonic Amplitudes. Figure 10 and Table 1 show the normalized harmonic amplitudes A_1, A_2, and A_3 versus damage in volts for the NLUT tests. Each datum in the table represents an average of the four directions tested through the concrete specimen. The values for each of the three specimens of a given water to cement ratio are averaged. This average value is then divided by the initial value at 0% damage to provide each specimen with the same initial value (1.000). Since the values of A_1, A_2, and A_3 have relatively the same scale when normalized, it is important to remember that A_3 is typically ten times smaller than A_2 and A_2 is typically ten times smaller than A_1. The table also shows the 95% confidence interval for the NLUT tests.

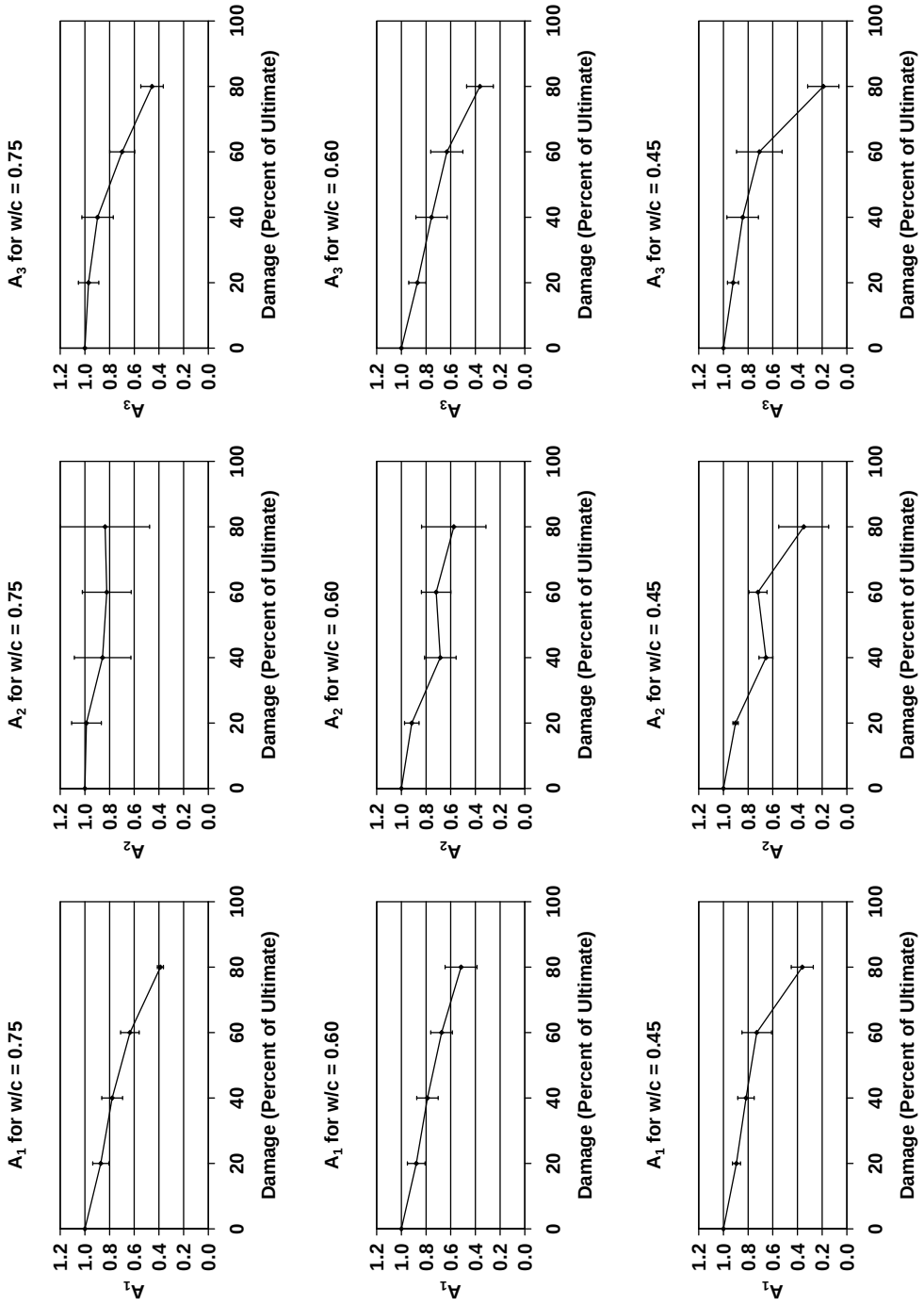

Figure 10. Normalized Harmonic Amplitudes (A_1, A_2, and A_3)

Table 1. Normalized Harmonic Amplitudes and Confidence Intervals

Specimen X (w/c = 0.75)						
Damage (Percent of Ultimate)	A1		A2		A3	
	Amplitude	CI	Amplitude	CI	Amplitude	CI
0	1	-	1	-	1	-
20	0.871	0.065	0.987	0.121	0.970	0.082
40	0.779	0.084	0.857	0.229	0.897	0.127
60	0.635	0.075	0.822	0.198	0.698	0.101
80	0.388	0.024	0.837	0.361	0.456	0.091
Specimen Y (w/c = 0.60)						
Damage (Percent of Ultimate)	A1		A2		A3	
	Amplitude	CI	Amplitude	CI	Amplitude	CI
0	1	-	1	-	1	-
20	0.880	0.072	0.916	0.058	0.870	0.071
40	0.789	0.087	0.685	0.128	0.755	0.127
60	0.674	0.087	0.718	0.119	0.632	0.130
80	0.516	0.130	0.576	0.261	0.363	0.108
Specimen Z (w/c = 0.45)						
Damage (Percent of Ultimate)	A1		A2		A3	
	Amplitude	CI	Amplitude	CI	Amplitude	CI
0	1	-	1	-	1	-
20	0.894	0.033	0.902	0.022	0.922	0.044
40	0.818	0.067	0.655	0.056	0.844	0.127
60	0.730	0.119	0.721	0.073	0.709	0.184
80	0.362	0.089	0.349	0.202	0.190	0.126

Discussion of Amplitude Trends. For all three water to cement ratios, a steady decline in fundamental, second, and third harmonic amplitudes is noted from 0% to 60% damage levels. The decline is somewhat sharper between 60% and 80% damage levels. The largest change noted for the fundamental amplitude is for the 0.45 water to cement ratio. This may be explained by the fact that capillary porosity is related to the water to cement ratio (Mindess et al. [2003]). Lower water to cement ratios have a lower initial porosity. Therefore, the 0.45 water to cement ratio has little initial porosity and the amplitudes for this water to cement ratio experience more drastic changes as the specimen is damaged when compared to the specimens of higher water to cement ratio.

There are two mechanisms responsible for the decrease in the amplitude of the fundamental signal. These mechanisms are attenuation of the fundamental signal and

conversion of the fundamental signal energy to higher harmonics. Attenuation effects are not evaluated in this research. However, the study of harmonic generation due to damage is an objective of this research.

The second harmonic experiences an overall drop in amplitude from 0% to 80% damage levels. A sharper drop in the amplitude is noted between the 60% and 80% damage levels. This sharp drop in amplitude is due to the increased presence of microcracks which attenuate the signal. Little, if any, conversion of this second harmonic to higher frequencies contributes to the decrease in signal strength because the power level of the second harmonic is probably too low. As with the fundamental signal, the largest change for the second harmonic amplitude is noted for the 0.45 water to cement ratio.

The behavior of the second harmonic differs from the fundamental signal in that between the 40% and 60% damage levels the second harmonic amplitude increases for the 0.60 and 0.45 water to cement ratios indicating a significant increase in damage. At these damage levels, the microcracking may be uniform to the point that the conversion of the fundamental signal to second harmonic actually becomes more efficient than the attenuative process of the cracks. Attenuation is a major cause for the decrease in signal strength for other stages of damage in the specimen, similar to the fundamental signal.

The third harmonic experiences a steady decline in amplitude from 0% to 80% damage levels, which is more similar to the fundamental signal than the second harmonic. As was seen with the fundamental signal and second harmonic, a sharper drop in signal strength is noted between the 60% and 80% damage levels. This decrease in signal strength is similar to the decrease in signal strength of the second harmonic and inferences can be drawn for the decrease in amplitude due to attenuation and conversion of the signal to harmonics as discussed for the second harmonic. As was the case for the fundamental and second harmonics, the largest drop in amplitude is noted for the 0.45 water to cement ratio.

As with the fundamental and second harmonics, the third harmonic experiences a drop in signal strength due to attenuation. However, the third harmonic is consistently attenuated more than the fundamental or second harmonics. Literature suggests that a wave can successfully pass through defects at or smaller in size than the propagating wavelength (Landis and Shah [1995]). For a fundamental frequency of 50 kHz, the fundamental wavelength is approximately three inches. The wavelengths of the second and third harmonics are then one and a half inches and one inch, respectively. The third harmonic is of a smaller wavelength and is affected by smaller defects more than the fundamental and second harmonics and is therefore attenuated more easily than the fundamental and second harmonics.

The NLUT harmonic ratio, pulse velocity, and resonant frequency methods are compared in terms of percent change. The percent change of each test is plotted on the y-axis as a function of damage plotted on the x-axis.

Figure 11 show the results of the 0.75 water to cement ratio. The graph show a marked difference in sensitivity between the methods. Both harmonic ratios show increases over 10% at the 20% damage level. The second harmonic appears to drop off somewhat at the 40% damage level. Large increases are noted with the NLUT harmonic ratios at the 60% and 80% damage levels.

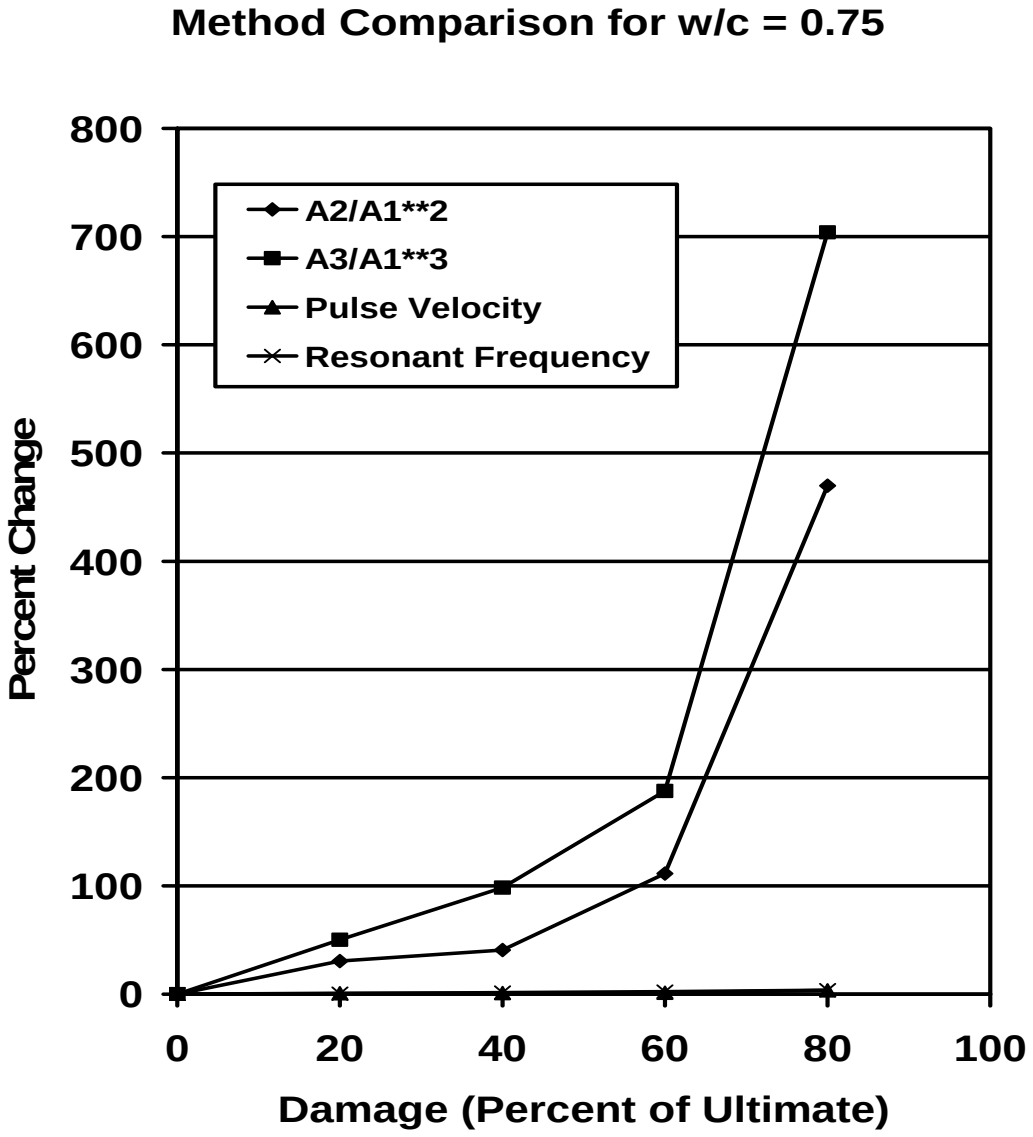

Figure 11. Damage Comparisons

The results of the ASTM methods show a sharp contrast in sensitivity from the NLUT [illegible] ne

20% damage level. The tests do show a steady increase from 0% to 80% damage levels with the largest percent change of 11% occurring with the resonant frequency method. Table 2 summarizes the comparison of percent changes in the methods as a result of damage.

Table 2. Method Comparison

w/c	Percent Damage	Percent Change			
		NLUT A_2/A_1^2	NLUT A_3/A_1^3	Velocity	Resonant
0.75	0	0	0	0	0
	20	31	50.21	0.74	0.39
	40	41	98.27	0.92	1.39
	60	111	187.73	1.30	2.19
	80	470	703.92	3.55	3.69
0.6	0	0	0.00	0.00	0.00
	20	19	29.98	0.23	0.40
	40	9.74	57.32	1.16	1.00
	60	58.80	109.85	1.35	1.77
	80	138.53	260.61	10.23	3.75
0.45	0	0.00	0.00	0.00	0.00
	20	12.90	29.17	0.96	0.52
	40	1.56	54.86	1.16	1.23
	60	42.09	86.13	2.41	2.24
	80	154.38	272.04	9.20	10.64

The research compared a nonlinear ultrasound method to two other established methods for the detection of early damage in concrete. The nonlinear ultrasound method was analyzed using the fundamental frequency (A_1), the second harmonic (A_2), and the third harmonic (A_3). Ratios of the normalized harmonic amplitudes were used (A_2/A_1^2 and A_3/A_1^3 versus damage, A_2 versus A_1^2, and A_3 versus A_1^3) to establish trends. Pulse velocity and resonant frequency methods were also tested for comparison.

The harmonic amplitudes (A_1, A_2, and A_3) decreased with increasing damage levels. Attenuation and conversion of the signal to higher harmonics due to internal defects decreased the amplitudes. The third harmonic experienced a greater decrease in amplitude than the fundamental signal due to the major difference in frequencies between the fundamental and third harmonic.

The harmonic ratios (A_2/A_1^2 and A_3/A_1^3) increased with increasing damage levels. Large variation was noted at the 80% damage level for most specimens where large cracks began to affect the signal. The third harmonic ratio (A_3/A_1^3) was consistently more sensitive to damage than the second harmonic.

The plots of A_2 versus A_1^2 and A_3 versus A_1^3 show increasing values of A_2 and A_3, respectively, with increasing damage. Literature suggests that the relationships are linear with homogeneous materials like ceramics. This research shows that the relationship is quadratic for A_2 versus A_1^2 and cubic for A_3 versus A_1^3. These relationships are consistent with nonhomogenous materials behavior.

The resonant frequencies decreased with increasing damage which follows current theory. The confidence intervals were generally small suggesting the method is highly repeatable. The pulse velocities decreased with increasing damage. This is explained by the increased path length around cracks that the signal must travel, thereby decreasing the velocity.

A distinction among the methods is made when considering the percent change of each method. At early damage levels (around 20% of the ultimate strength) the nonlinear method was consistently more sensitive than the pulse velocity and resonant frequency methods. The nonlinear ultrasound method becomes even more sensitive than the other methods as the concrete becomes more damaged.

Based on the findings of the work, the following conclusions are made:

1. The performance of NLUT to detect early damage in concrete significantly exceeded ASTM methods C 215 and C 597 even at the first damage increment corresponding to a load of 20% of the ultimate strength of the concrete.

2. The ASTM methods were generally insensitive to damage up to about 60% of the ultimate strength of the concrete.

3. The normalized third harmonic ratio (A_3/A_1^3) was consistently more sensitive to damage than the normalized second harmonic ratio (A_2/A_1^2) independent of water-cement ratio.

5. Load Factor Calibration and Analysis.

This research reports on the strength evaluation of the I-40 Bridge, a precast, prestressed concrete girder bridge that carries the east and westbound traffic on Interstate-40 (I-40) over the Rio Grande River in Albuquerque, New Mexico. During the past seven years that the I-40 Bridge has been in service, a large number of overweight vehicles have been denied an overload permit. These permit decisions were made by the New Mexico Department of Transportation (NMDOT) and were based on the results of a capacity rating analysis. If denied a permit, the designated detour typically results in about 8.0 km (5 miles) and 30 minutes of additional travel on city streets for the truck driver. This change in itinerary is an inconvenience to the trucking industry that results in detour related expenses. Hence, the primary objective of this study was to determine a more accurate capacity level for the I-40 Bridge, one which better represented the true capacity

of the bridge so that the NMDOT would avoid unnecessarily rejecting a permit request for an overweight vehicle.

In this study, a systematic approach was followed to arrive at a more accurate capacity rating for the I-40 Bridge. A conventional rating analysis was first performed based on the LFD (Load Factor Design) Method specified in the AASHTO (American State Highway and Transportation Officials) Manual for Condition Evaluation of Bridges (2000). To confirm and possibly further improve the LFD load rating, a diagnostic load test and a detailed finite-element analysis of the I-40 Bridge were completed. Details of the LFD rating analysis as well as the procedures for integrating girder strain measurements from the load test and finite-element results into the capacity rating of the bridge are discussed.

Bridge Description. The I-40 Bridge consists of twin structures that carry eastbound and westbound traffic over the Rio Grande River. Each structure is composed of a series of three precast, prestressed concrete bridges (two 3-span continuous bridges separated by a 4-span continuous bridge) that span a total distance of 378 m (1240 ft). The two exterior bridges are 3-span continuous bridges with span lengths of 39.4, 30.5 and 39.6 m (129 ft 2 in, 100 ft, and 130 ft). A 4-span continuous bridge with equal span lengths of 39.6 m (130 ft) is located between the two 3-span bridges. The bridge was designed based on the LFD Method given in the AASHTO Standard Specifications. Construction of the I-40 Bridge was completed in 1995, at which time it replaced a fracture-critical, plate girder steel bridge that had previously been in service for approximately 30 years.

Figures 12 and 13 each show a design drawing and photograph (looking west) of the exterior 3-span continuous bridge unit located on the eastern end of the westbound structure. The three spans are supported by fixed (labeled F) and expansion (labeled E) bearings as shown in Figure 12(a). The cross-section of the I-40 Bridge consists of twelve bulb tee BT-1830 (BT-72) girders spaced 2.2 m (7 ft 3 in) apart as shown in Figure 12(a).

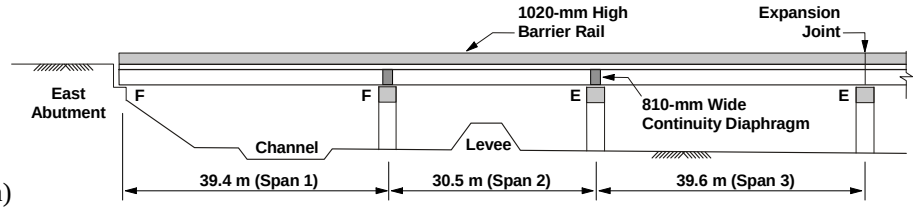

(a)

(b)

Figure 12. Longitudinal view of the I-40 Bridge: (a) design drawing and (b) photograph from underneath.

(a)

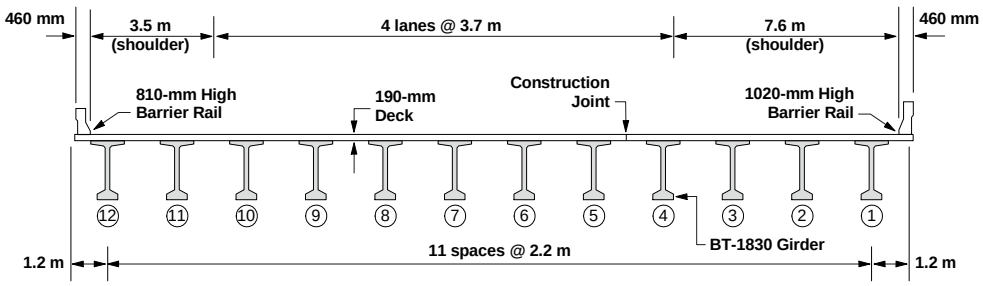

(b)

Figure 13. Cross-sectional view of the I-40 Bridge: (a) design drawing and (b) photograph from topside.

The girders were designed as simple spans for non-composite dead loads (including the girder self-weight, slab / haunch weight, stay-in-place metal decking, and diaphragms) and as continuous spans under composite dead loads (including the future wearing surface and traffic barriers) and vehicular live load. Structural continuity under composite dead loads and live load was achieved at the interior piers by providing cast-in-place closure diaphragms and negative moment reinforcement in the deck slab. The girders were designed to act composite with a 191-mm (7 ½-in) thick, reinforced concrete

deck. The concrete compressive strengths for the girders were specified as 37 MPa (5400 psi) at release and 41 MPa (6000 psi) at 28 days. A 28-day concrete compressive strength of 21 MPa (3000 psi) was specified for the deck. A dead load allowance of 1.4 kPa (30 psf) for a future wearing surface was also considered in the design.

Conventional Load Rating Analysis. In accordance with NMDOT bridge design provisions, engineering consultants are required to specify an inventory (INV) and operating (OPR) rating for the bridge. The decision to issue a permit is primarily made based on a comparison between the maximum bending moment caused by the overload vehicle ($M_{overload}$) and the maximum bending moment caused by HS-20 truck loading (M_{HS-20}). A permit is granted if the moment ratio ($M_{overload}$ / M_{HS-20}) does not exceed the OPR rating factor for the bridge. When the moment ratio is greater than the OPR rating factor, the bridge is considered unsafe to carry the overload and the vehicle is rerouted along an alternate route. Before this study was performed, the original load ratings for the I-40 Bridge were INV = 1.00 and OPR = 1.67.

Based on the flexural capacities of the girders, separate load ratings were determined for the 3 and 4-span continuous bridge units of the I-40 Bridge. Load ratings were determined for an interior and exterior girder in both the positive and negative moment regions. In the LFD method (AASHTO, 2000), a rating factor is determined using the equation

$$RF = \frac{R_n - \gamma_D D}{\gamma_L L(1+I)}$$

where RF = bridge load rating factor (either operating or inventory); R_n = nominal member capacity (based on flexural strength); γ_D = dead load factor = 1.3; D = nominal dead load effect (including non-composite and composite dead loads); γ_L = live load factor = 1.3 (for operating rating) and 2.17 (for inventory rating); L = nominal live load effect (caused either by HS-20 truck or lane loading); and I = live load impact factor = 15.24 / (L + 38) where L is the individual span length (taken as 39.6 m) = 0.196 (equal to zero for lane loading). The inventory rating is the smaller of the two rating levels and is defined in the AASHTO Manual for Condition Evaluation of Bridges (2000) as the "live load that can safely utilize an existing structure for an indefinite period of time". The operating rating factor corresponds to the "maximum permissible live load to which a structure may be subjected" (AASHTO, 2000) but on a limited basis such as an occasional overweight vehicle. The rating factors represent the multiple of the force effects caused by either the HS-20 vehicle or lane loading that the bridge can safely carry at the inventory and operating levels. For example, an operating rating factor equal to 3 (computed based on the live load effects caused by HS-20 loading) indicates that the bridge can safely carry a vehicular load that causes a bending moment equal to three times that caused by HS-20 loading.

The magnitudes of flexural capacity, dead load moments (non-composite and composite), and live load moments were computed according to the AASHTO Standard Specifications (1996) using information taken from the design drawings of the I-40

Bridge. Both the positive and negative moment regions of the 3 and 4-span continuous bridge units were evaluated. For each bridge unit, the critical section for positive moment occurred close to mid-span of the 39.6 m (130 ft) exterior span, while the critical negative moment section occurred at the interior support of the exterior span. The LFD rating analysis was first performed for an interior girder and rating factors were computed for HS-20 vehicular loading and lane loading. For positive moment, the 4-span bridge had slightly smaller rating factors (INV = 1.93 and OPR = 3.22) under HS-20 vehicular loading compared to the 3-span bridge which had rating factors of INV = 1.96 and OPR = 3.28. The rating factors computed for lane loading were about 25% higher than those computed for HS-20 loading and thus, HS-20 loading controlled for positive moment. In the negative moment region, the rating factors were smaller for the 3-span bridge (INV = 2.03 and OPR = 3.38) than the 4-span bridge (INV = 2.61 and OPR = 4.36) based on HS-20 vehicular loading. When lane loading was considered, however, the factors decreased to roughly INV = 1.70 and OPR = 2.85 for both the 3 and 4-span bridges. These rating factors were found to be the smallest magnitudes and thus, represented the new load capacity of the I-40 Bridge at the inventory and operating levels (note that the original ratings were INV = 1.0 and OPR = 1.67).

To complete the LFD rating analysis, an exterior girder was also evaluated. The exterior girders had the same prestressing strand layout as the interior girders, but an effective flange width approximately 76 mm (3 in) larger. For rating purposes, this small difference in the effective flange width was ignored and exterior girder parameters (including the flexural capacity and dead load moments) were assumed to be equal to those for the interior girder. One major difference between the two girders, however, was the load distribution factor. The AASHTO Standard Specifications (1996) states that the load distribution factor for bending moment of an exterior girder “shall be determined by applying to the stringer or beam the reaction of the wheel load obtained by assuming the flooring to act as a simple span between stringers or beams”. This approach, also known as the lever rule concept, resulted in a distribution factor for the exterior girder equal to 0.632. For the interior girder, AASHTO (1996) specifies a distribution factor of (S / 5.5) where S is the average girder spacing in feet, which amounted to 0.659. Since the load distribution factor was smaller for the exterior girder, which results in smaller live load moments, and the reserve strength (i.e., flexural capacity minus dead load moments) was about the same for both girders, the exterior girder had larger rating factors than the interior girder and thus, did not control the load rating.

Nondestructive Live Load Testing. Although not usually considered in design, certain attributes of bridge behavior have been observed in numerous load tests to favorably influence the load distribution and safe load-carrying capacity of slab-on-girder bridges. Some of the factors that affect bridge performance include end restraint, unintended continuity, flexural participation of curbs and/or railings, and two-way slab action (Burdette and Goodpasture, 1988). The standard AASHTO LFD rating procedure, however, employs concepts and assumptions similar to those used in design, which ignore these factors and thus, often underestimate the bridge’s true capacity. As a result, several state highway departments have adopted non-destructive load testing to better quantify the response of a bridge to live load. Starting in the 1980’s, the New York

Department of Transportation has occasionally used load testing to determine the safe load level for a bridge. In the last ten years, experimental bridge rating activity has expanded to other state departments of transportation such as Florida (Shahawy, 1995) and Alabama (Conner et al., 1997). Outside the U. S., the Ontario Ministry of Transportation in Canada has extensive experience in bridge testing (Bakht and Jaeger, 1990).

The two types of non-destructive load tests commonly used to evaluate the live load response of an existing bridge are diagnostic and proof tests. These two methods differ in terms of the level of load applied to the bridge, the quantity and significance of measurements taken, and the manner in which the experimental findings are used to arrive at a load rating (Lichtenstein, 1998; Pinjarkar, 1998). In a diagnostic test, the bridge is subjected to a known load below its elastic load limit or *Diagnostic Test Load* as shown in Figure 14.

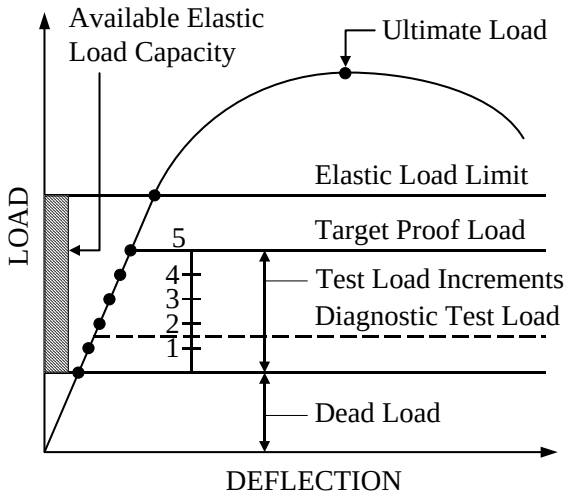

Figure 14. Hypothetical load-deflection response of a bridge (adapted from Pinjarkar, 1998).

Strain and/or deflection measurements are taken at strategic locations to determine the load distribution and stiffness characteristics of the bridge. Following the test, the measurements are then used in combination with an analytical model to confirm the behavior of the bridge and better estimate its capacity. In a proof test, increasing loads (labeled 1 through 5 in Figure 14) are applied to the bridge until a *Target Proof Load* is reached or non-linear behavior is observed. When either of these two events occurs, the load test is stopped and the maximum load carried by the bridge is adjusted to determine the load rating. In both the diagnostic and proof test, the measurements can be used to adjust or refine the load rating of the bridge.

A diagnostic load test was performed since it could be completed in less time than a proof test and the design plans of the I-40 Bridge were available to create a representative analytical model. Furthermore, two of the four lanes could be left open to traffic during the diagnostic load test and a smaller truck could be used to apply

load. A proof test typically requires closing all the lanes on the bridge until completion of the test, which was not an option on the interstate and also involves applying large levels of load in a careful and time-consuming manner. Strain transducers were installed on eight of the twelve girders at two longitudinal locations along the 3-span bridge unit; close to the interior support or negative moment region and at the mid-span or positive moment region (labeled *NEG* and *POS*, respectively, in Figure 15(a)). This particular bridge unit was considered the most practical for load testing because of its easy access and low vertical clearance compared to the other bridge units. The instrumentation locations proved to be the most accessible since there was a catwalk installed at the interior pier and a levee at mid-span (see Figure 13). At both locations, a pair of strain transducers was installed on girders 1 through 8; on the bottom of the girder and below the top flange as shown in Figure 15(b). This instrumentation layout resulted in a total of 32 strain measurements (16 at each instrumented section).

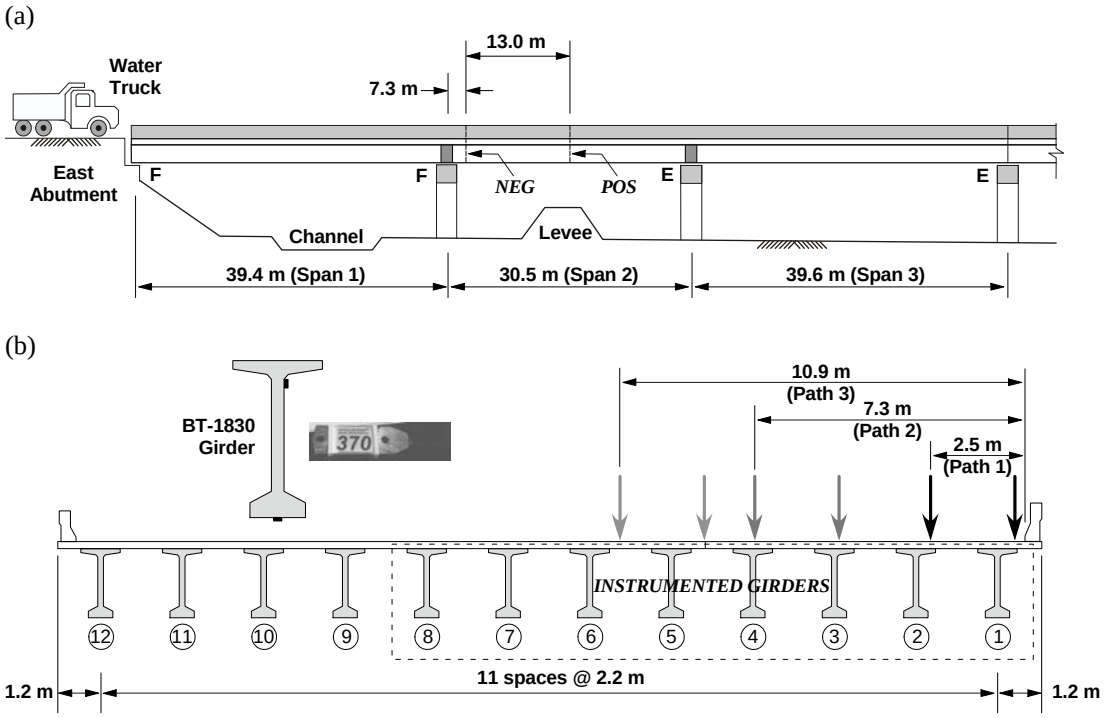

Figure 15. Diagnostic load test setup of the I-40 Bridge: (a) longitudinal view and (b) cross-sectional view at instrumented locations, *POS* and *NEG*.

Using a 16-channel data acquisition system, the bridge was tested over a two-day period with a six-person crew starting with the positive moment region. Traffic control was arranged through the NMDOT, which involved closing the two north lanes of the I-40 Bridge and leaving the two south lanes open to traffic (refer to Figure 13 for lane positions). A single, three-axle water truck weighing 238 kN (53.4 kips) was used to apply load to the bridge since it was the heaviest vehicle the NMDOT could provide at the time of testing. The truck was driven over the entire length of the 3-span bridge

starting at the east abutment at a speed of approximately 8 kph (5 mph) along three separate paths. Each truck pass was completed with either minimal or no traffic on the open lanes. To ensure good data records, three separate runs were completed for each truck path. Strain measurements were collected at a rate of 32 Hz. With the truck traveling at approximately 8 kph (5 mph), a typical run required a total time of approximately 1 minute. As a result, there were instances when there was normal traffic on the tested bridge while the water truck was on course along the load path. If a large truck was on the bridge during a test, the test was redone until three tests were completed free of heavy truck traffic to avoid affecting the girder strain measurements. Due to the time of the test, passenger cars and trucks were seldom present and had very little effect on the recorded girder strains.

Figure 16 shows the average top and bottom strains (from three separate runs) recorded at the positive moment region of the exterior girder. For this truck path, the exterior girder was the most heavily loaded girder and as a result, had the largest recorded change in strain. The figure shows that when the truck was in the first or third span, the mid-span moment in the second span was negative. When the truck was in the second span, the moment is positive and largest when the truck was near mid-span. These trends confirmed that the bridge was acting as a continuous system; however, the degree of continuity was not obvious solely from the strain record.

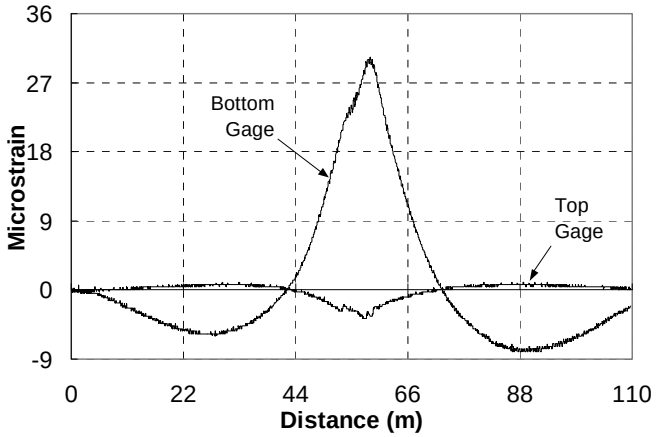

Figure 16. Average measured strain response at mid-span of exterior girder.

Furthermore, since the location of the top gage was near the neutral axis of the composite girder (as computed based on a transformed section analysis), the small compression strains in the top gage and the large tensile strains in the bottom gage indicated that the girder and deck were acting composite and no unexpected loss of composite action had occurred. The averaged measured neutral axis was within 5% of the calculated composite neutral axis based on material properties determined using the design concrete strengths and tributary width recommended by AASHTO. Similar trends were recorded for the other instrumented girders for each load path in both the positive and negative

moment regions. These observations related to the general behavior of the I-40 Bridge were used to develop an analytical model (which incorporated both continuity and composite action) for the finite-element analysis.

Finite Element Analysis. A finite-element model of a concrete slab-on-girder bridge can be created in many different ways. The modeling scheme developed by Zokaie et al. (1991) was adopted because it was relatively simple and it was also used in the development of the live-load distribution factor equations given in the AASHTO (1998) Load and Resistance Factor Design Specifications. Hence, the precast girders were modeled using frame elements placed at their geometric centroid and the bridge deck was modeled using four-node shell elements. Because the centroids of the girder and deck are not coplanar, rigid-body constraints were enforced to connect the two separate components and simulate composite action. Figure 17 shows a cross-sectional view of the frame and shell finite-element model.

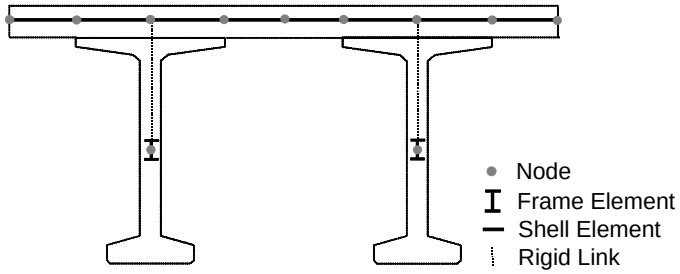

Figure 17. Finite-element modeling scheme of the I-40 Bridge.

The measured live-load response of the 3-span bridge test was compared with the theoretical response calculated with three finite-element models. In the first model (labeled CONTINUOUS), the 3-span bridge was supported with conventional pins at the fixed bearing locations and rollers at the expansion bearing locations. This model ignored the effect of pier stiffness on the bridge response. In the second bridge model (labeled FRAME), the four circular columns of the interior piers were modeled with frame elements to simulate the actual pier stiffness. For the third bridge model (labeled FIXED), the ends of the girders in the second span were fixed (i.e., no translation and no rotation) at the interior pier locations. This model was intended to represent an upper bound on the interior pier stiffness.

Finite-element output generated by the bridge models included axial forces and moments for the frame elements (girder), and top and bottom stresses for the shell elements (deck). Composite, cross-sectional moments for the interior and exterior girders were found by first calculating the stress at the bottom of the girder caused by the theoretical forces in the frame element. The resulting stress was then multiplied by the theoretical, composite section modulus to obtain the girder moment. The measured composite, cross-sectional bending moments in the girders from the live-load test were calculated as the product of the change in strain (with the bridge in its loaded and unloaded condition), the modulus of elasticity, and the theoretical, composite section modulus.

Figure 18 compares the positive mid-span moments for the exterior girder calculated from the measured strain values (labeled TEST) with those determined from the three finite-element models discussed earlier. The figure shows that the CONTINUOUS model overestimated the absolute value of the measured mid-span moment when the truck was on any of the three spans. The maximum positive moment from this model was about 34% larger than the mid-span moment measured from the live-load test. The FIXED model produced moments that were close to the measured moments when the truck was on the second span; however, since the girder deformations were restrained at the ends of the second span, the truck loading on the first or third span caused no bending moment at mid-span, which did not agree with the live-load test. This model was intended to provide an upper limit on the rotational stiffness at the pier and yielded mid-span moments that were nearly 8% smaller than the measured moments with the truck on the second span. The FRAME model provided a good correlation between the measured and predicted moment values when the truck was in all three spans. The mid-span moment from this model was slightly larger (by about 3%) than the measured moment. This strong correlation between the measured moment and those from the FRAME model was observed for each girder and for each load case. Although the interior piers were not designed to produce this type of restrained behavior, the pier stiffness contributed to measured moments about 25 percent smaller than those calculated based on design assumptions (i.e., pin and roller supports or zero pier stiffness).

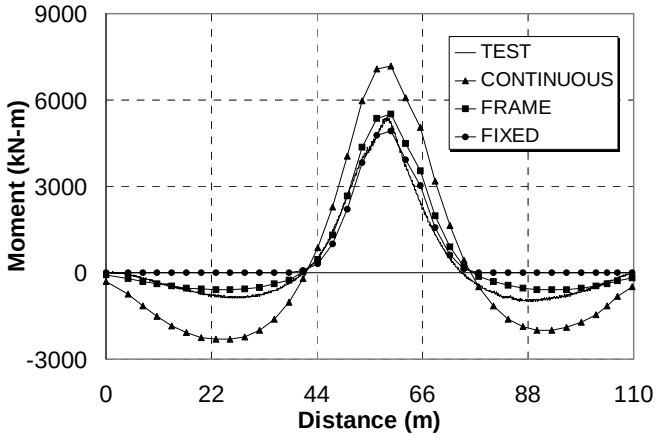

Figure 18. Measured vs. finite element moments at mid-span of exterior girder.

Figure 19 (a) shows a comparison of the mid-span moments for girders 1 through 8 with the truck positioned at the critical location for maximum positive moment along the first path. The finite-element moments plotted in the figure were calculated using the FRAME model. Figure 19(b) shows the same comparison as that given in Figure 20(a) with the truck positioned transversely in the second path. Similar to the first path, there was a close correlation (within 6%) between the finite element and the measured moments, which confirmed the accuracy of the FRAME model.

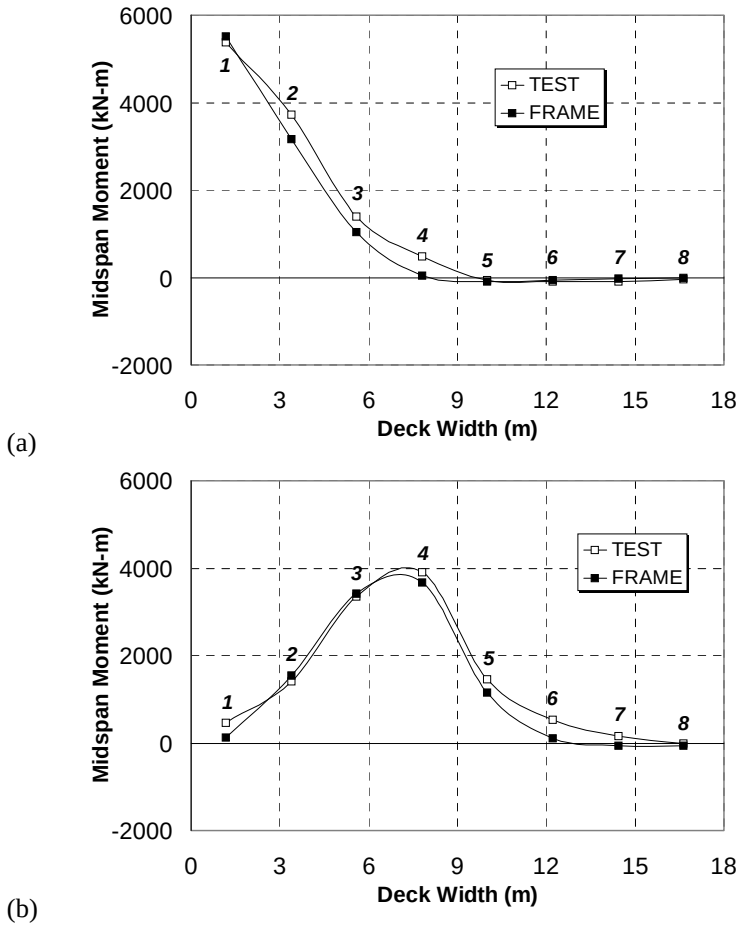

Figure 19. Measured vs. finite element moments at mid-span of the I-40 Bridge: (a) first path and (b) second path.

Research has shown that the AASHTO based distribution factor can be overly conservative and can differ significantly compared to finite-element results. As a result, the FRAME and CONTINUOUS finite-element models of the I-40 Bridge were used in lieu of the AASHTO Standard equation to obtain more accurate live-load distribution factors. Although including the columns in the FRAME model decreased the total moment at mid-span by about 25 percent as discussed earlier, the pier stiffness did not significantly influence (i.e., there was a less than 5% difference in the values between the CONTINUOUS and FRAME models) the load distribution between the girders in the transverse direction. In comparison to the AASHTO Standard distribution factors (i.e., 0.659 for the interior girder and 0.632 for the exterior girder), the finite-element values were constantly smaller. The differences between the finite-element and AASHTO distribution factors ranged from 3 to 13%.

Compared to the rating factors determined using the AASHTO Standard distribution factors, the rating factors determined based on finite-element results were larger. For positive moment, the new rating factors were 15% and 9% larger, while for negative moment, the rating factors were only 10% and 3% larger for the interior and exterior girders, respectively. These percentages indicate that the AASHTO Standard distribution

factor was the most conservative in the case of positive moment of an interior girder. In this case, the finite-element distribution factor of 0.575 was well below the AASHTO distribution factor of 0.659, which resulted in the large increase of 15% in the load rating factors. The cases of positive moment of an exterior girder and negative moment of an interior girder showed about the same improvement (10%) in the rating factors. For negative moment of an exterior girder, however, the distribution factors from AASHTO (0.632) and the finite-element model (0.615) correlated very well and as a result, there was not a significant change in the rating factors (i.e., only 3%). Thus, the distribution factors from the finite-element analysis of the I-40 Bridge further verified the AASHTO Standard distribution factors but did not result in any significant improvements beyond the AASHTO LFD capacity ratings. However, the 25% reduction in the longitudinal moment caused by the pier stiffness may improve the capacity ratings even more but was not investigated further in this research.

Conclusions. A load rating analysis was performed on the I-40 Bridge over the Rio Grande River in Albuquerque, New Mexico. The analysis showed that the inventory and operating factors of the I-40 Bridge could be increased by a factor of 1.7 to 1.70 and 2.85, respectively. A diagnostic load test was performed to validate this increase in the capacity ratings. The results of the load test showed that the stiffness of the interior piers affected the longitudinal distribution of live load. The pier stiffness resulted in a mid-span moment that was about 25 percent smaller than the moment a designer would obtain assuming the girders were supported by pins and rollers. A finite-element model of the bridge was then used to calculate a more accurate live-load distribution factor. The finite-element analyses resulted in distribution factors ranging from 3% to 15% smaller than the AASHTO Standard distribution factors. Results of the finite-element analysis also showed that the pier stiffness did not have a significant influence on the value of the distribution factor. No significant changes occurred in the rating factors as a result of the finite-element distribution factors; however, the reduction in the longitudinal moment in the girders caused by the stiffness at the interior piers may improve the capacity ratings. Based on these findings, the New Mexico Department of Transportation (NMDOT) safely increased the inventory and operating ratings of the I-40 Bridge to 1.70 and 2.85, respectively.

References

American Association of State Highway and Transportation Officials (AASHTO) (2000), *Manual for condition evaluation of bridges*, 2nd Edition, Washington, AASHTO.

American Association of State Highway and Transportation Officials (AASHTO) (1998), *LRFD bridge design specifications*, 2nd Edition, Washington, AASHTO.

American Association of State Highway and Transportation Officials (AASHTO) (1996), *Standard specifications for highway bridges*, 16th Edition, Washington, AASHTO.

Bakht B and Jaeger L G (1990), 'Bridge testing – a surprise every time', *ASCE Journal of Structural Engineering*, 116 (5), 1370–1383.

Burdette E G and Goodpasture D W (1988), *Correlation of bridge load capacity estimates with test data*, NCHRP Report 306, Washington, Transportation Research Board.

Conner G H, Stallings J M, McDuffie T L, Campbell J R, Fulton R Y, Shelton B A, and Mullins R B (1997), 'Bridge load testing in Alabama', *76th Transportation Research Board Meeting*, Washington.

Lichtenstein A G (1998), *Manual for bridge rating through load testing*, Research Results Digest 234, Washington, Transportation Research Board.

Pinjarkar S G (1998), 'An overview of current worldwide practices for nondestructive load testing for bridge rating and evaluation', *Proceedings of the 5th Annual International Bridge Conference*, IBC-88-11, 25–31.

Shahawy M A (1995), 'Nondestructive strength evaluation of Florida bridges', *Proceedings of SPIE – The International Society of Optical Engineering (Nondestructive Evaluation of Aging Bridges and Highways)*, 2456, 101–123.

Zokaie T, Oserkamp T A, and Imbsen R A (1991), *Distribution of wheel loads on highway bridges*, NCHRP Report 12-26, Washington, Transportation Research Board.